Fluids and Barriers of the CNS

RESEARCH

Open Access

CSF dynamics throughout the ventricular system using 4D flow MRI: associations to arterial pulsatility, ventricular volumes, and age

Tomas Vikner[1,2], Kevin M. Johnson[1,3], Robert V. Cadman[4,5], Tobey J. Betthauser[4,5], Rachael E. Wilson[4,5], Nathaniel Chin[4,5], Laura B. Eisenmenger[3], Sterling C. Johnson[4,5] and Leonardo A. Rivera-Rivera[1,4,5*]

Abstract

Background Cerebrospinal fluid (CSF) dynamics are increasingly studied in aging and neurological disorders. Models of CSF-mediated waste clearance suggest that altered CSF dynamics could play a role in the accumulation of toxic waste in the CNS, with implications for Alzheimer's disease and other proteinopathies. Therefore, approaches that enable quantitative and volumetric assessment of CSF flow velocities could be of value. In this study we demonstrate the feasibility of 4D flow MRI for simultaneous assessment of CSF dynamics throughout the ventricular system, and evaluate associations to arterial pulsatility, ventricular volumes, and age.

Methods In a cognitively unimpaired cohort ($N=43$; age 41–83 years), cardiac-resolved 4D flow MRI CSF velocities were obtained in the lateral ventricles (LV), foramens of Monro, third and fourth ventricles (V3 and V4), the cerebral aqueduct (CA) and the spinal canal (SC), using a velocity encoding (venc) of 5 cm/s. Cerebral blood flow pulsatility was also assessed with 4D flow (venc = 80 cm/s), and CSF volumes were obtained from T1- and T2-weighted MRI. Multiple linear regression was used to assess effects of age, ventricular volumes, and arterial pulsatility on CSF velocities.

Results Cardiac-driven CSF dynamics were observed in all CSF spaces, with region-averaged velocity range and root-mean-square (RMS) velocity encompassing from very low in the LVs (RMS 0.25 ± 0.08; range 0.85 ± 0.28 mm/s) to relatively high in the CA (RMS 6.29 ± 2.87; range 18.6 ± 15.2 mm/s). In the regression models, CSF velocity was significantly related to age in 5/6 regions, to CSF space volume in 2/3 regions, and to arterial pulsatility in 3/6 regions. Group-averaged waveforms indicated distinct CSF flow propagation delays throughout CSF spaces, particularly between the SC and LVs.

Conclusions Our findings show that 4D flow MRI enables assessment of CSF dynamics throughout the ventricular system, and captures independent effects of age, CSF space morphology, and arterial pulsatility on CSF motion.

*Correspondence:
Leonardo A. Rivera-Rivera
larivera@medicine.wisc.edu

Full list of author information is available at the end of the article

Keywords Magnetic resonance imaging, 4D flow MRI, Cerebrospinal fluid, Cerebral blood flow, Flow dynamics, Cardiac pulsatility

Background

Neurofluid dynamics are of interest to advance our understanding of brain physiology, aging, cognitive decline, and the pathophysiology of neurological disorders. Cerebrospinal fluid (CSF) and interstitial fluid dynamics, and their exchange, seem to play key roles for removal of toxic metabolic waste from the CNS [1]. In Alzheimer's disease (AD) and idiopathic normal pressure hydrocephalus (INPH), altered cerebral blood flow [2, 3] (CBF) and CSF dynamics [4, 5] may develop as a consequence of disease progression. Further, as suggested by animal studies and models of CSF-mediated waste clearance systems (e.g., glymphatics [1]), altered CSF dynamics and reduced CBF-to-CSF coupling [6, 7] may impair the brain's ability remove toxic waste products including amyloid-β, potentially contributing to proteinopathies such as AD. However, these observations need verification in humans. Importantly, translation from animal to human studies rely on non-invasive imaging methods capable of assessing neurofluid dynamics.

In the last decades, human magnetic resonance imaging (MRI) studies have significantly improved our understanding of CSF circulation and the role of altered CSF dynamics in neurological disorders [8]. For instance, velocity-sensitive 2D phase contrast (PC) MRI studies have derived non-invasive intracranial compliance [9] and pressure [10, 11] estimates, and have revealed a tight coupling between CBF and CSF flow dynamics by comparing arterial inflow to CSF flow and venous outflow at the cervical spine [12, 13], reflecting the near-rigid properties of the cranium [14] (Monro-Kellie hypothesis [15]). Further, cardiac-gated 2D PC measures of CSF stroke volume [4, 16] and CSF flow direction [17, 18] in the cerebral aqueduct (CA) have shown useful as additional diagnostic criteria for INPH and other CSF disorders. More recently, real-time 2D PC has been used to assess the effects of free breathing on both blood [19] and CSF [20, 21] flow fluctuations. Quantitative 2D PC MRI provides high spatiotemporal resolution and test-retest reliability [22]; however, due to lack of volumetric coverage most 2D PC studies on CSF dynamics have been limited to spinal canal (SC) and CA.

4D flow MRI (time-resolved volumetric PC MRI with 3-directional velocity encoding) has emerged as a powerful extension of 2D PC MRI enabling volumetric measures of neurofluid dynamics. Previous 4D flow MRI studies have linked multiple cerebral hemodynamic parameters to aging [3, 23], small vessel disease [23, 24] and AD [3, 25, 26], including arterial pulsatility [3, 23], pulse wave velocity [24, 25] (PWV), and low frequency oscillations [26]. More recently, applications of 4D flow MRI to study CSF dynamics have also emerged [27] (4D CSF flow MRI), associating altered intracranial CSF dynamics with hydrocephalus [28–31] and AD [29, 30]. Further, spinal 4D CSF flow MRI have shown potential for diagnostic aid in Chiari malformations [32, 33], accelerated by compressed sensing [34]. Yet, 4D flow studies on intracranial CSF dynamics are scarce, and the effects of age, CSF space volumes and CBF dynamics on CSF motion have not been well-established throughout most of the ventricular system.

Here, cardiac-resolved 4D flow MRI is used to assess CSF velocities along the ventricular system in multiple regions of interest (ROIs), including the lateral ventricles (LV, L/R), foramens of Monro (FMo, L/R), third ventricle (V3), CA, fourth ventricle (V4), and the spinal canal (SC). The root-mean-square (RMS) velocity and the velocity range are used to provide descriptive characteristics of CSF dynamics in the various CSF compartments, and stroke volume is also assessed for the CA. To provide further understanding of the mechanisms that influence CSF dynamics, CSF velocities are evaluated in relation to age, ventricle and CSF space morphology from structural MRI, and in relation to cerebral arterial hemodynamics, also obtained by 4D flow MRI.

Materials and methods

Participants

Data were analyzed from participants of the Wisconsin Registry of Alzheimer's Prevention [35] (WRAP). The investigated cohort consisted of middle-aged to older (N=43; age 41 to 83 years; mean age 67±7.5 years; 27 female) participants that were cognitively unimpaired as determined from multidisciplinary consensus conference [36–41] and AD biomarker negative from PET [42] and/or plasma [43] at the time of the 4D flow MRI scans. The University of Wisconsin Institutional Review Board approved all study procedures and protocols following the policies and guidance established by the campus Human Research Protection Program (HRPP). Each participant signed a written informed consent before participation.

Magnetic resonance imaging

MRI data were acquired on a 3.0T system (SIGNA Premier, GE Healthcare) using a 48-channel head-coil (GE Healthcare).

Structural MRI

3D T1-weighted anatomical images were acquired using an MPRAGE sequence with field of view (FoV) 25.6×25.6×20.8 cm^3 and 1 mm isotropic spatial resolution. T2-weighted anatomical images were acquired using a cardiac-gated, flow-compensated CUBE sequence with a FoV of 25.0×25.0×20.5 cm^3 and 1.0×1.0×1.6 mm^3 spatial resolution.

4D flow MRI of CSF

4D flow MRI of CSF was acquired using a Cartesian based product sequence with prospective cardiac gating using a peripheral photoplethysmography (PPG) (GE Healthcare) sensor worn on the participant finger. Imaging was performed sagittal with a FoV set to cover the spinal canal and ventricular spaces. Relevant parameters included: FoV=24.0×4.0×24.0 cm^3, acquired resolution=1.0 mm isotropic (interpolated to 0.5 mm), TR/TE=12/7 ms, flip angle=3°, prospectively cardiac-gated (10–15 frames collected per cardiac cycle; interpolated to 20), velocity encoding (Venc)=5 cm/s, k-t acceleration using Kat-ARC=8. The scan time was ~10 min but varied slightly based on heart rate, with a cohort-averaged heart rate of 66±9.7 bpm. Example images from a 4D CSF flow MRI scan are shown in Fig. 1.

4D flow MRI of CBF

A radially undersampled 4D flow acquisition was used for the assessment of CBF hemodynamics [44, 45]. Imaging parameters: acquisition FoV=22×22×16 cm^3, TR/TE=8.6/ 2.5 ms, number of projections ~ 11,000, scan time=5.6 min, acquired spatial resolution=0.7 mm isotropic, flip angle=8°, and Venc=80 cm/s. Retrospectively gated cardiac-resolved images were reconstructed offline to 20 cardiac phases using cardiac triggers recorded during the MRI scan using peripheral PPG.

Image analysis

Preprocessing

From the CSF 4D flow MRI scans, a reference anatomical image was derived by temporal averaging of the magnitude volumes (20 frames per cardiac cycle). FreeSurfer (v6.0.0) with the T1-weighted volumes as input was used for segmentation of the CSF space into the third (V3), fourth (V4), and lateral (LV) ventricular subregions [46]. The T1- and T2-weighted scans, and the FreeSurfer segmentations, were then resampled and co-registered to the 4D CSF flow magnitude reference using rigid-body registration and a normalized mutual information (NMI) cost function in SPM12. In addition, SPM12 was used to segment CSF probability maps from the co-registered T2-weighted to further refine and assure minimal

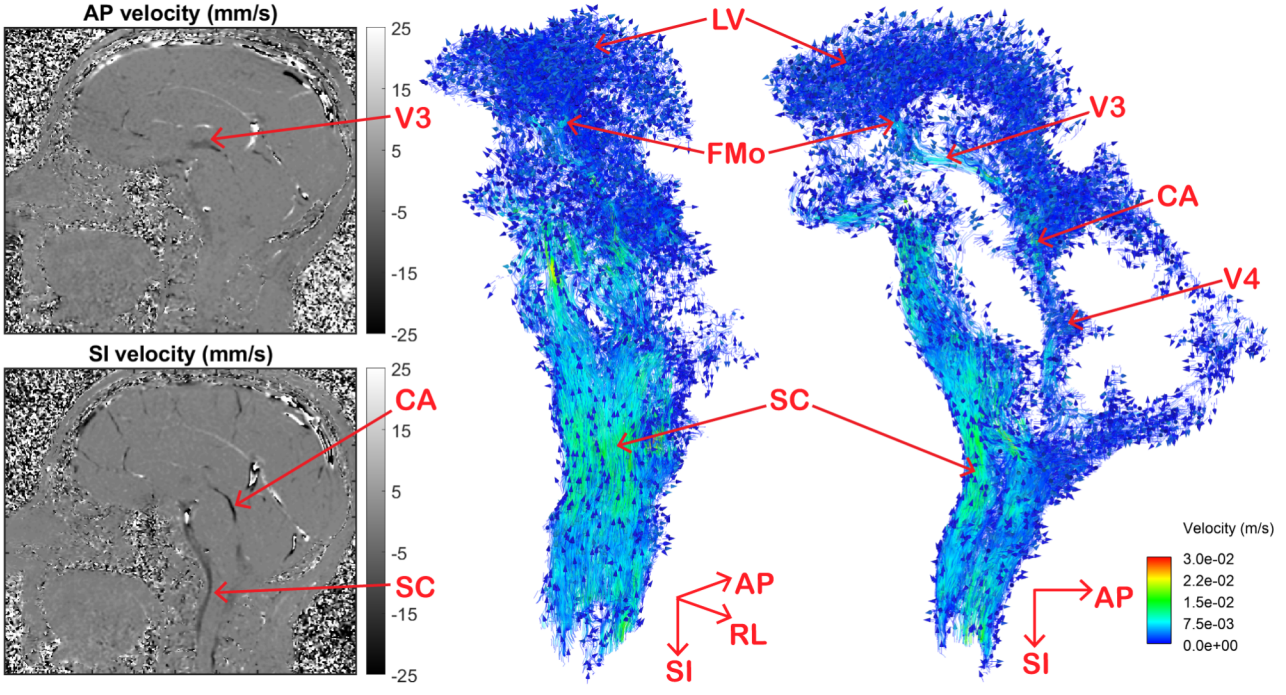

Fig. 1 Velocity images from a 4D flow MRI scan of cerebrospinal fluid (CSF) shown in the sagittal plane (left) in the anterior-posterior (AP) and superior-inferior (SI) velocity directions at late diastolic phase of the cardiac cycle, indicating CSF inflow in the third ventricle (V3), the cerebral aqueduct (CA) and the spinal canal (SC). Velocity streamlines (right) were generated from the same 4D flow dataset using Ansys EnSight (2022R2) at the same cardiac cycle time frame as the left velocity images. Cardiac-resolved visualizations of the same dataset are provided in the supplementary material (Sup. Vid. 1; Sup. Vid. 2). Note that the streamline figure in the middle represents a 45-degree rotation of the right figure around the vertical (SI) axis. RL, right-left; V4, fourth ventricle; FMo, foramen of Monro; LV, lateral ventricle

inclusion of tissue in the FreeSurfer defined ROIs. Velocity data from 4D flow scans for CSF and CBF were corrected for phase offsets using 2nd order polynomial fits to the background field [47] and velocity anti-aliasing [48].

Ventricular segmentation

The LVs (left and right), V3, and V4 were obtained from the automatic FreeSurfer segmentations, multiplied with a CSF mask derived from SPM12 segmentations of the T2 weighted volumes (CSF probability > 0.95). For the 4D flow MRI analyses, CSF ROIs were also eroded one voxel to minimize the influence of partial volume effects.

Foramen of Monro segmentation

The foramen of Monros (FMo, left and right) were defined by considering the LV and V3 intersection, using an iterative region-growing approach. For each iteration, the dilated LV and V3 segments were multiplied with a CSF mask (CSF probability > 0.95) to avoid false connections between the LVs and V3.

Cerebral aqueduct segmentation

The CA was segmented using semi-automatic segmentations based on user-defined seed points, a contrast mask from a root-mean-square (RMS) velocity map divided by the 4D flow magnitude (RMS./Mag) as input, followed by region-growing and intensity thresholding. Manual segmentations of the CA were also obtained using GyroTools GTFlow (4.9).

Spinal canal segmentation

The SC was automatically segmented using T2 intensities over a 2.5 cm coverage at the C2/C3 level of the cervical spine, using an initial intensity-threshold of 50% of max within the slice range, and a one voxel erosion to reduce partial volume effects.

CSF waveform analysis

Velocity waveforms in the anterior-posterior (AP), left-right (LR), and superior-inferior (SI) directions were sampled from the 4D flow MRI data for all CSF voxels. For each CSF ROI, principal component analysis (PCA) was used to estimate a single velocity waveform defined as the first principal component (PC1) (MATLAB, MathWorks). This was done by first obtaining individual AP, LR, and SI waveforms by spatial averaging across all voxels within the ROI, and using the AP, LR and SI waveforms as input to the PCA. Similar waveforms were also obtained when using AP, LR, and SI waveforms sampled from all ROI voxels as input to the PCA (Sup. Figure 2). Since CSF velocities average to near zero over the cardiac cycle, the final waveforms were characterized by the root-mean-square (RMS) velocity and velocity range (maximum velocity – minimum velocity). The CA stroke volume ($\triangle$V; µl/cardiac cycle) was calculated for the CA as the range (systolic max – diastolic min) of the cumulative integral of the CA flow rate waveform [12] after segmentation in GTFlow. Velocity streamlines (Fig. 1; Sup. Vid. 1; Sup. Vid. 2) were obtained in Ansys EnSight (2022R2).

4D flow CBF waveform analysis

Arterial waveforms were sampled at the left and right internal carotid arteries (ICAs), the left and right middle cerebral arteries (MCAs), and the basilar artery (BA), using a validated semi-automatic MATLAB based tool (https://github.com/uwmri/QVT) [49]. One total cerebral blood flow (tCBF) waveform was then defined by adding the ICA and BA waveforms, and single ICA and MCA waveforms were also defined by adding the right and left ICAs and MCAs, respectively. The tCBF rate (ml/min) was estimated from the tCBF waveform, and arterial volume pulsatility ($\triangle$V * heart rate) and the pulsatility index (PI) were estimated from the ICA and the MCA waveforms. Arterial volume pulsatility ($\triangle$V * heart rate; ml/min) was calculated as the range of the cumulative integral of the cardiac flow rate waveform after subtracting the mean flow [12], but was also multiplied by heart rate to achieve volume pulsations in units of ml/min. The PI was defined as the flow range (systolic max – diastolic min) divided by the mean flow rate over the cardiac cycle.

Statistical analysis

Multiple linear regression (MLR) was also used to model RMS velocity (mm/s) in CSF as a function of age (years), CSF volumes (ml), and arterial volume pulsatility (ml/min). The RMS velocities were approximately normally distributed (skewness 0.21 to 1.10; kurtosis −0.72 to 0.72) for all ROIs, and regression coefficients (β) from the MLR models were standardized by z-score (i.e. all input variables had zero mean and standard deviation one). Linear (Pearson) correlation was used to assess relations between CBF dynamics and age. CA stroke volume was not normally distributed (skewness 1.59); hence, Spearman's ρ was used to evaluate CA stroke volume in relation to ventricular volume. P-values < 0.05 were considered significant.

Results

Cardiac-pulsatility could be measured from 4D flow MRI data in all the investigated CSF compartments, as indicated by the group-averaged PC1-velocity waveforms (Fig. 2) and the group-averaged AP-, LR-, and SI-velocity waveforms (Sup. Figure 3). The average (±1SD) variance explained by the PC1-waveform was highest for the SC (99 ± 1.0%) and lowest for the LVs (75 ± 9.4), and between 89 and 99% for the other CSF ROIs. Time-resolved

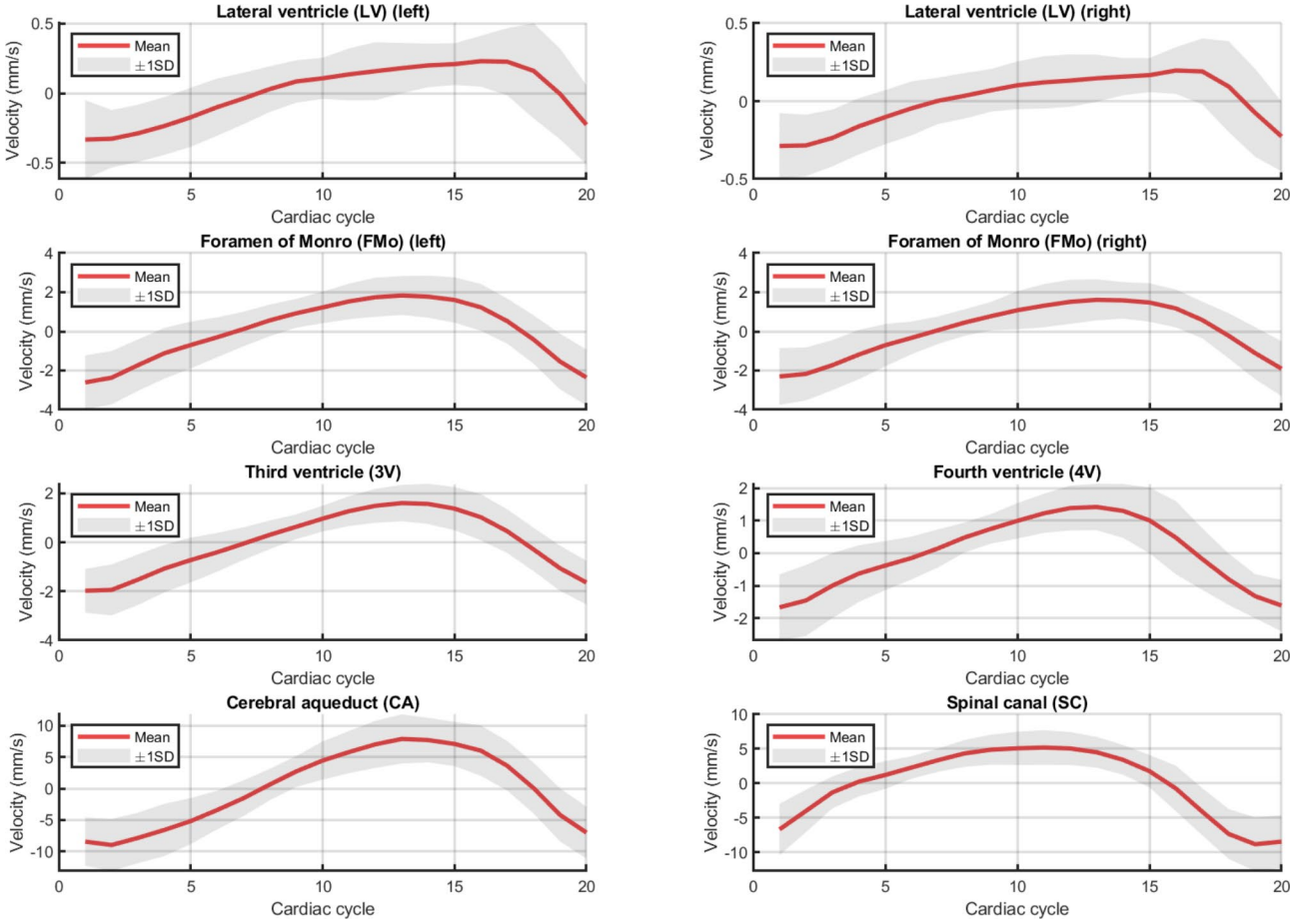

Fig. 2 Cardiac-resolved CSF velocity waveforms in all CSF ROIs averaged over the entire cohort ($N=43$), with shaded regions representing ± 1 standard deviation (SD). The individual velocity waveforms were defined as the first principal component (PC1) of the ROI-averaged x-, y-, and z-velocity components. Note that positive velocities indicate CSF inflow to the brain (in the SC-to-LV direction), and negative velocities indicate CSF outflow due to CSF being pushed out by the inflow of blood during the systolic phase of the cardiac cycle. The cohort-average heart rate was 66 ± 9.7 bpm

Table 1 CSF morphology and CSF velocity characteristics of the cohort ($N=43$)

CSF region	CSF vol. (ml)	CSF frac. (%)	RMS vel. (mm/s)	Vel. range (mm/s)
Whole-brain	199 ± 33.4	100 ± 0	NA	NA
Lateral ventricles	23.2 ± 12.6	11.3 ± 4.91	0.25 ± 0.08	0.85 ± 0.28
Foramen of Monro	NA	NA	1.59 ± 0.70	4.88 ± 2.14
Third ventricle	1.34 ± 0.52	0.66 ± 0.20	1.33 ± 0.60	3.98 ± 1.83
Cerebral aqueduct	NA	NA	6.29 ± 2.87	18.6 ± 15.2
Fourth ventricle	1.59 ± 0.41	0.81 ± 0.21	1.20 ± 0.54	3.62 ± 1.65
Spinal canal	NA	NA	5.10 ± 2.08	15.2 ± 5.87

Note CSF volumes were segmented using FreeSurfer (lateral, 3rd, and 4th ventricles) and SPM (whole brain). The CSF fraction (%) was estimated by dividing the regional CSF volume by the whole-brain CSF volume. The CSF velocities were assessed by root-mean-square (RMS) and range, calculated from the region-averaged CSF waveforms. For some of the regions, CSF volume or velocity was not assessed, indicated by not applicable (NA)

visualizations of the CSF pulsations are provided in the supplementary material (Sup. Vid. 1–2).

Group-averaged CSF velocities were lowest in LVs (range: 0.85 ± 0.28 mm/s; RMS: 0.25 ± 0.08 mm/s) and highest in the CA (range: 18.6 ± 15.2 mm/s; RMS: 6.29 ± 2.87 mm/s) (Table 1), indicating a wide range of CSF velocities among regions. Within the group, region-averaged velocity ranges extended from 0.46 to 1.96 mm/s in the LVs and 2.55 to 34.1 mm/s in the CA, and RMS velocities from 0.14 to 0.49 mm/s the LVs and 0.85 to 12.36 mm/s in the CA (Sup. Figure 4), also indicating high inter-individual variability in CSF dynamics.

Simultaneous visualization of the group-averaged PC1 CSF waveforms indicated that the systolic outflow and diastolic inflow velocity peaks appear first in the SC, later in the V4, and finally in the LVs (Fig. 3). However, the CA, V3 and FMo waveform peaks appeared relatively concomitantly, likely reflecting a limited ability to resolve small time delays with the current temporal resolution.

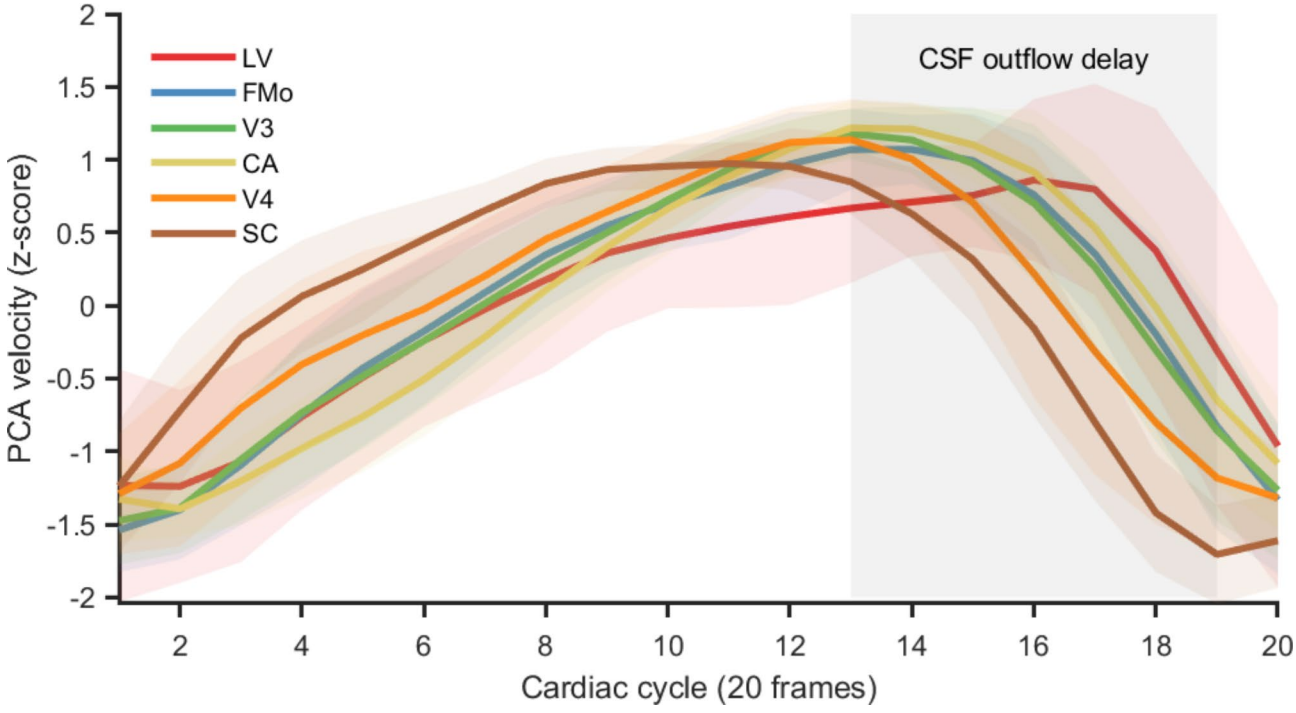

Fig. 3 Timing differences in inflow and outflow among CSF spaces, indicating that CSF outflow during the systolic phase of the cardiac cycle starts in the (SC), followed by the 4th ventricle (V4), then relatively concomitantly in the cerebral aqueduct (CA), 3rd ventricle (V3) and foramen of Monro (FMo), and finally in the lateral ventricles (LV) with an outflow delay difference of about 3 frames (~140 ms) from the SC. Note that negative PCA velocity here indicates CSF outflow (which occurs several times frames after the systolic onset), due to CSF being pushed out by the inflow of blood. The PC1 waveforms displayed here were averaged over the entire cohort ($N=43$), with shaded regions reflecting ± 1 standard deviation, and *z*-scored to facilitate visualization on different velocity scales

Table 2 Cerebral blood flow characteristics of the cohort ($N=43$) and relations to age

Vessel (s)	Mean ± SD	Correlation to age
tCBF* (ml/min)	491 ± 103	r = -0.30; $p=0.051$
ICA Δ V (ml/min)	52.3 ± 11.4	$r=0.25$; $p=0.10$
ICA PI	1.09 ± 0.19	$r=0.63$; $p<0.001$***
MCA ΔV (ml/min)	31.9 ± 7.67	$r=0.18$; $p=0.26$
MCA PI	1.13 ± 0.22	$r=0.58$; $p<0.001$***

Note *The total cerebral blood flow (tCBF) waveform was calculated as the sum of the internal carotid artery (ICA, left and right) and basilary artery waveforms. MCA, middle cerebral artery; ΔV, arterial volume pulsatility; PI, pulsatility index

Table 3 CSF velocity relations to age, CSF volume and CBF pulsatility using multiple linear regression

RMS vel. (mm/s)	Effect of age	Effect of CSF volume	Effect of CBF pulsatility
Lateral ventricle	β = -0.42; $p<0.001$***	β = -0.47; $p<0.001$***	β = 0.29; $p=0.020$*
Foramen of Monro	β = 0.41; $p=0.007$**	NA	β = 0.11; $p=0.44$
3rd ventricle	β = 0.39; $p=0.013$*	β = -0.40; $p=0.012$*	β = 0.24; $p=0.093$
Cerebral aqueduct	β = 0.34; $p=0.029$*	NA	β = 0.06; $p=0.69$
4th ventricle	β = 0.30; $p=0.035$*	β = 0.19; $p=0.16$	β = 0.31; $p=0.030$*
Spinal canal	β = -0.07; $p=0.65$	NA	β = 0.39; $p=0.012$*

Note The β represents a standardized estimate. The effect of CSF volumes corresponds to local CSF space volume of the corresponding ROI (i.e., where velocities were analyzed). Effect of CBF pulsatility corresponds to arterial volume pulsatility (ΔV; ml/s) in the MCA

Total cerebral blood flow rate (tCBF) was 491 ± 103 ml/min (Table 2), with a borderline-significant inverse relation to age (r=-0.30; $p=0.051$). Further, arterial PI showed pronounced age-relations ($r=0.63$ and $r=0.58$ for ICA and MCA; $p<0.001$) and a PI-increase of approximately 1.5%/year, whereas arterial volume pulsatility (ΔV) showed non-significant positive age-trends ($r=0.25$, $p=0.10$ for ICA; $r=0.18$, $p=0.26$ for MCA).

Since CSF velocity ranges and RMS velocities were very highly correlated ($R=0.95$ to $R=0.99$) for all CSF ROIs (Sup. Figure 4), only RMS velocities were considered in multiple linear regression (MLR) models. The MLR results indicated an age-related increase in CSF velocity for most ROIs (FMo, V3, CA, V4), but an age-related decrease for the LVs, as well as inverse CSF space volume-velocity relationships in the LVs and V3 (Table 3). Further, in 3/6 ROIs (LV, V4, SC), there was an expected positive CBF-CSF dynamics association, whereas the others showed non-significant positive trends.

Stroke volume in the CA ranged from 1.32 to 49.5 (13.7 ± 11.6) µl per cardiac cycle (Fig. 4), indicating very large interindividual variability. Stroke volume was also evaluated against ventricular volume (Sup. Figure 5), showing a positive association (ρ=0.53; p < 0.001).

Discussion

We demonstrated the feasibility of 4D flow MRI as a method for simultaneous, quantitative assessment of cardiac-related CSF dynamics throughout the ventricular system. We further provided descriptive values of RMS velocities and velocity ranges across multiple ROIs in a cognitively healthy aging cohort. As an initial study, we also showed 4D CSF flow MRI dynamics to be influenced by age, CSF space morphology, and cardiac-related CBF pulsations. These findings provide valuable data to inform future studies on disease progression, including information to aid in the selection of imaging parameters (e.g. Venc) and inform the overall study design (e.g. controlling for age, CSF volumes, and CBF). Our studies also highlight the potential of 4D flow MRI to investigate CSF flow changes associated with aging, altered CBF-CSF coupling, INPH, AD, among other neurological disorders.

Cardiac pulsatility was measurable in all CSF compartments with a venc of 5 cm/s, although the presence of noise was much more prominent in the LVs compared to other CSF spaces, as both indicated by the waveforms (Fig. 2) and by the variance explained by the first principal component (i.e., ~75% in the LVs vs. 99% in the SC). Considering that region-averaged LV ranges were <1 mm/s on average, the protocol velocity encoding of 5 cm/s is likely sub-optimal for this CSF space. Stadlbauer et al. [28] reported 4D flow dynamics in the LVs with maximum peak velocities of 7.6 ± 2.2 mm/s; however, the study does not describe the landmark location for the LV measurements (e.g. inlet plane vs. region-averaged), which can largely influence the reported velocities. In our study, we observed a substantially lower region-averaged velocity range (0.85 ± 0.28 mm/s), but high peak velocities could still be observed in single voxels (~ 20 mm/s). While LV velocities may be high near the inlet, complex flow patterns and high variability in velocity within the LVs can be expected, creating a challenge to define standardized landmarks for velocity measurements. Nevertheless, the current 5 cm/s setting appeared suitable for high-velocity compartments such as SC and CA, and still managed to capture ventricular dynamics related to age, ventricle volume, and CBF pulsations. Previous 4D CSF flow studies have selected widely different velocity encodings depending on the application, with most studies ranging from 5 to 20 cm/s [27]. Future 4D CSF flow MRI studies should consider lower or dual-venc settings suitable for the LVs velocities.

CSF velocity increased with age in 4/6 regions (FMo, V3, CA, V4), whereas an inverse age-relation was found for the LVs. In a previous study comparing INPH patients with hypermotile CSF flow to controls, INPH patients showed elevated velocities in V4, CA, V3 and FMo, whereas no differences where observed in LV velocities between the groups [28]. The regression model in our study included age, LV volume and arterial volume pulsatility, suggesting an age-effect independent of ventricular expansion, or a non-linear effect such as altered tissue mechanics properties. Regarding the CBF-CSF associations, a significant positive relation was found in 3/6 CSF regions (LV, V4, SC), supporting the notion that CBF pulsations drive CSF flow motion. Previous studies have shown a close relationship between the CSF waveform and the difference between the arterial inflow and

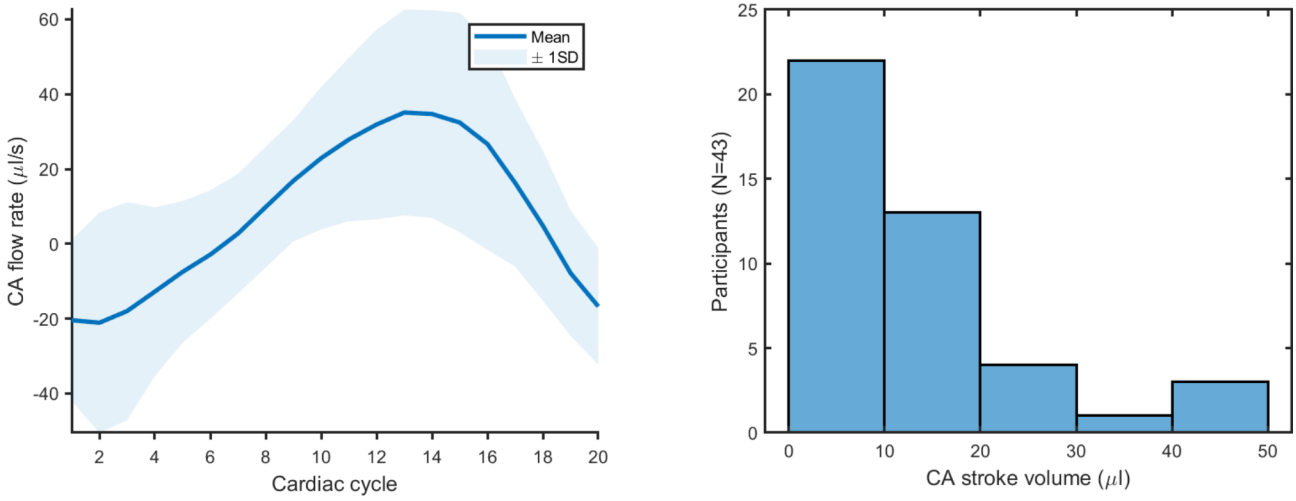

Fig. 4 Group-averaged cerebral aqueduct (CA) CSF flow waveform after manual segmentations performed in GyroTools GTFlow, with patched region corresponding to ± 1 standard deviation (SD). The average stroke volume was 13.7 ± 11.6 µl per cardiac cycle from N = 43 participants

the venous outflow waveforms, reflecting the near-rigid properties of the skull [14, 15]. Further, a 2D PC MRI study found high correlation (r=0.75) when comparing arterial inflow vs. jugular vein plus CSF outflow in the cervical spine [12]. The smaller effects of CBF pulsations on CSF velocities in our data (β=0.06 to 0.39, or r=0.06 to 0.38) may partially be attributed to the lower temporal resolution of the 4D CSF flow scan (prospectively gated with 10–15 cardiac phases) compared to the CBF 4D flow scan (retrospectively gated to 20 cardiac phases), and partially due to the lack of jugular vein measurements (e.g. venous outflow).

In line with previous findings, arterial PI increased with age, with approximately 1.5% per year; a relatively large effect compared to previous cross-sectional [50] and longitudinal [23] age-effects of 1.0-1.2%. The large age-PI effect and the borderline-significance of the age-tCBF effect likely reflects the small sample size of the current study. However, no age-association was found for the arterial volume pulsatility measures. This likely reflects that while △V goes up as blood flow becomes more pulsatile with older age, the age-related tCBF decline causes a concomitant reduction in △V. Hence, the net effect of age on △V is expected to be relatively small.

CSF velocities were mainly assessed using principal component analysis with region-averaged AP, LR, and SI velocity waveforms as input, although flow rate (μl/min) and stroke volume (μl) using cross-sectional cut planes were also assessed for the CA. While defining orthogonal planes is straightforward for some CSF ROIs (e.g., the SC and CA), positioning of planes is less obvious for larger CSF spaces [51] (V4, V3, and LVs). Further, segmentation of tight conduits (FMo and CA) could cause partial volume errors with relatively large impact on flow rates. In contrast to CBF studies where semi-automatic flow tools [49] are evaluated and easily accessible, a combination of fully automatic (FreeSurfer) and semi-automatic in-house tools was used for CSF segmentation, potentially causing some user-dependent variability. With an increasing number of studies showing the feasibility of CSF dynamics imaging, post-processing tools for CSF segmentation and CSF motion analysis need to be developed and evaluated. In the CA, the region-averaged velocity range was 18.6±15.2 mm/s, which was surprisingly far below the venc (50 mm/s). Using 2D PC MRI, Eide et al. observed min and max velocities of -44.6 and 36.9 mm/s in the CA of the reference group [18] and Lee et al. observed peak systolic velocities of 33.0±16.1 to 40.7±20.2 mm/s along CA segments of healthy volunteers [52]. Moreover, our CA stroke volumes of 13.7±11.6 μl were also relatively low compared to 2D PC studies by Balédent et al. [13] (51±25 μl), Wåhlin et al. [12] (32±19 μl) and Sakhare et al. [22] (38±17 μl). Our relatively low CA velocities and stroke volumes compared to other 2D PC studies can potentially be attributed to our lower spatial and temporal resolutions (1.0 mm acquired voxel size; 10–15 acquired frames/cycle), making it difficult to detect peak velocities in narrow conduits. Furthermore, region-averaging and PCA filtering of the CSF waveforms also likely contributes to our observed lower velocity measurements (compared to 2D planes). A recent 4D flow MRI study also underestimated velocities compared to 2D studies, reporting velocity amplitudes in the upper and lower CA of 7.8±5.0 mm/s and 9.4±7.0 mm/s respectively [31]. To understand these discrepancies, PC MRI studies characterizing the sources contributing to 4D flow and 2D PC CSF velocity differences are warranted. Nevertheless, in our study CA velocities and stroke volume were related to age and ventricular volume, agreeing with previous findings [53].

The group-averaged CSF waveforms also indicated time delays between subsequent ROIs, with spinal CSF peaks preceding the other CSF peaks, with a particularly long delay (~140ms or ~15% of the cardiac cycle) to the lateral ventricles. Similar delays were also reported in a 2D PC study of young participants (27±4 years) by Balédent et al., observing short propagation times between arterial and spinal peaks (~5% of the cardiac cycle), and relatively long delays (~21% of the cardiac cycle) between arterial flow and the aqueduct, corresponding to a CSF flow delay of ~16% from the SC to the CA [13]. The slightly higher propagation speed in our study may partially be attributed to an elderly cohort. One 4D flow study used correlation mapping and a reference region approximately at the basilar artery level to assess CSF propagation to the V4, V3 and LVs, with age-dependent time delays corresponding to 7.03–12.01% and 4.56–5.22% of the cardiac cycle in healthy young and elderly, respectively [54]. These relatively small time delays compared to our data and Balédent et al. [13] are likely attributed to a difference reference region, further superior in the intracranial CSF space. Overall, it is plausible that CSF outflows from SC first during systole due its location at the interphase between the cranium and the neck, where blood inflows to the cranial cavity, and in a similar fashion CSF inflows first through the SC as it returns from the body to the cranium during diastole.

This study has a few limitations. Different 4D flow sequences were used to study CBF and CSF dynamics, partially because of challenges associated with the longer T1 of CSF and utilization of a sagittal acquisition to image the CSF ventricular space. Further, the CBF 4D flow scan had higher temporal resolution than the CSF 4D flow scan (retrospective vs. prospective cardiac gating), leading to broadening of the CSF waveform peaks. Moreover, the spatial coverage of the CBF scan was optimized for the circle of Willis arteries and did not capture jugular veins blood flow, making it difficult to assess total

venous outflow. Hence, venous flow was not considered in this study. Furthermore, CBF and CSF dynamics were collected in separate scans, potentially leading to heart rate variability between scans. Together, this limited the study of CBF-CSF coupling. Finally, only cardiac gating (i.e., no real-time or respiratory gating) was considered in the current study, making it impossible to detect low-frequency CSF dynamics induced by slow vasomotion [55] or respiration [20, 21, 56]. Assessment of low-frequency CSF dynamics using 4D flow is challenged by the low velocities and long T1 times of CSF, likely leading to prohibited scan times. While real-time and/or respiratory gated 4D flow approaches should be explored leveraging recent advancements in hardware, acquisition and reconstruction, real-time 2D PC approaches are likely better suited, albeit with limited coverage.

In conclusion, 4D flow MRI is feasible for assessing cardiac-related CSF velocities throughout the ventricular system in a single scan. Like for CBF pulsatility, cardiac-related CSF dynamics increased with age for most CSF compartments, although the LVs showed an inverse age-association. In multiple linear regression models, CSF velocity could be described as a function of age, CSF morphology, and arterial volume pulsatility. These findings suggest a complex relationship where multiple factors influence CSF flow dynamics, something that needs to be considered in future studies attempting to elucidate the role of CSF dynamics in the context of brain aging and neurological disorders.

Supplementary Information

The online version contains supplementary material available at https://doi.org/10.1186/s12987-024-00570-4.

Supplementary Material 1

Supplementary Material 2

Supplementary Material 3

Acknowledgements
We acknowledge GE Healthcare for assistance and support.

Author contributions
T.V., K.M.J, and L.R.R conceptualized the 4D flow MRI experiments and analyzed the data. R.V.C., T.J.B., R.E.W., N.C., L.B.E., and S.C.J, contributed to data acquisition and interpretation of the data. T.V., K.M.J., and L.R.R. drafted the manuscript which was edited and approved by all authors.

Funding
Grant support was provided by the National Institutes of Health (R01AG075788, R01AG027161, R01AG021155, R01AG082208, P30AG062715, R21AG077337, R21NS125094, KL2TR002374, and UL1TR002373), the Alzheimer's Association (AARFD-20-678095), and the Swedish Brain Foundation (PS2023-0047).

Data availability
The datasets used and/or analyzed during the current study are available from the corresponding author on reasonable request.

Declarations

Ethics approval and consent to participate
The University of Wisconsin Institutional Review Board approved all study procedures and protocols following the policies and guidance established by the campus Human Research Protection Program (HRPP). Each participant signed a written informed consent before participation.

Consent for publication
Not applicable.

Competing interests
Sterling C. Johnson served on an advisory board for Roche Diagnostics in 2018 for which he received an honorarium and is principal investigator of an equipment grant from Roche. He conducts tau imaging in NIH funded studies as well as a study funded by Cerveau Technologies using radioligand precursor material supplied by Cerveau Technologies.

Author details
[1]Department of Medical Physics, School of Medicine and Public Health, University of Wisconsin-Madison, Madison, WI 53792, USA
[2]Department of Diagnostics and Intervention, Umeå University, Umeå S-90187, Sweden
[3]Department of Radiology, School of Medicine and Public Health, University of Wisconsin-Madison, Madison, WI 53726, USA
[4]Wisconsin Alzheimer's Disease Research Center, School of Medicine and Public Health, University of Wisconsin-Madison, Madison, WI 53792, USA
[5]Department of Medicine, School of Medicine and Public Health, University of Wisconsin-Madison, Madison, WI 53792, USA

Received: 9 May 2024 / Accepted: 19 August 2024
Published online: 30 August 2024

References

1. Nedergaard M, Goldman SA. Glymphatic failure as a final common pathway to dementia. Science. 2020;370(6512):50–6. https://doi.org/10.1126/science.abb8739.
2. Iturria-Medina Y, Sotero RC, Toussaint PJ, Mateos-Pérez JM, Evans AC. Early role of vascular dysregulation on late-onset Alzheimer's disease based on multifactorial data-driven analysis. Nat Commun. 2016;7(1):11934. https://doi.org/10.1038/ncomms11934.
3. Rivera-Rivera LA, Turski P, Johnson KM, et al. 4D flow MRI for intracranial hemodynamics assessment in Alzheimer's disease. J Cereb Blood Flow Metab. 2016;36(10):1718–30. https://doi.org/10.1177/0271678X15617171.
4. Bradley WG, Scalzo D, Queralt J, Nitz WN, Atkinson DJ, Wong P. Normal-pressure hydrocephalus: evaluation with cerebrospinal fluid flow measurements at MR imaging. Radiology. 1996;198(2):523–9. https://doi.org/10.1148/radiology.198.2.8596861.
5. El Sankari S, Gondry-Jouet C, Fichten A, et al. Cerebrospinal fluid and blood flow in mild cognitive impairment and Alzheimer's disease: a differential diagnosis from idiopathic normal pressure hydrocephalus. Fluids Barriers CNS. 2011;8(1):12. https://doi.org/10.1186/2045-8118-8-12.
6. Mestre H, Tithof J, Du T, et al. Flow of cerebrospinal fluid is driven by arterial pulsations and is reduced in hypertension. Nat Commun. 2018;9(1):4878. https://doi.org/10.1038/s41467-018-07318-3.
7. van Veluw SJ, Hou SS, Calvo-Rodriguez M, et al. Vasomotion as a driving force for paravascular clearance in the awake mouse brain. Neuron. 2020;105(3):549–e5615. https://doi.org/10.1016/j.neuron.2019.10.033.
8. Mehta NH, Suss RA, Dyke JP, et al. Quantifying cerebrospinal fluid dynamics: a review of human neuroimaging contributions to CSF physiology and neurodegenerative disease. Neurobiol Dis. 2022;170:105776. https://doi.org/10.1016/j.nbd.2022.105776.
9. Tain RW, Bagci AM, Lam BL, Sklar EM, Ertl-Wagner B, Alperin N. Determination of Cranio-spinal canal compliance distribution by MRI: methodology and early application in idiopathic intracranial hypertension. J Magn Reson Imaging JMRI. 2011;34(6):1397–404. https://doi.org/10.1002/jmri.22799.
10. Alperin NJ, Lee SH, Loth F, Raksin PB, Lichtor T. MR-Intracranial pressure (ICP): a method to measure intracranial elastance and pressure noninvasively by means of MR Imaging: Baboon and Human Study. Radiology. 2000;217(3):877–85. https://doi.org/10.1148/radiology.217.3.r00dc42877.

11. Alperin N, Lee SH, Bagci AM. MRI measurements of intracranial pressure in the upright posture: the effect of the hydrostatic pressure gradient. J Magn Reson Imaging JMRI. 2015;42(4):1158–63. https://doi.org/10.1002/jmri.24882.
12. Wåhlin A, Ambarki K, Hauksson J, Birgander R, Malm J, Eklund A. Phase contrast MRI quantification of pulsatile volumes of brain arteries, veins, and cerebrospinal fluids compartments: repeatability and physiological interactions. J Magn Reson Imaging JMRI. 2012;35(5):1055–62. https://doi.org/10.1002/jmri.23527.
13. Balédent O, Henry-Feugeas MC, C &, acuteeCILE I-PI. Cerebrospinal Fluid Dynamics and Relation with Blood Flow: a magnetic resonance study with Semiautomated Cerebrospinal Fluid Segmentation. Invest Radiol. 2001;36(7):368.
14. Alperin N. Does the brain have mechanical compliance? Magn Reson Mater Phys Biol Med. 2020;33(6):753–6. https://doi.org/10.1007/s10334-020-00880-2.
15. Mokri B. The Monro–Kellie hypothesis. Neurology. 2001;56(12):1746–8. https://doi.org/10.1212/WNL.56.12.1746.
16. Yamada S, Tsuchiya K, Bradley WG, et al. Current and emerging MR imaging techniques for the diagnosis and management of CSF flow disorders: a review of phase-contrast and time-spatial labeling inversion pulse. AJNR Am J Neuroradiol. 2015;36(4):623–30. https://doi.org/10.3174/ajnr.A4030.
17. Lindstrøm EK, Ringstad G, Mardal KA, Eide PK. Cerebrospinal fluid volumetric net flow rate and direction in idiopathic normal pressure hydrocephalus. NeuroImage Clin. 2018;20:731–41. https://doi.org/10.1016/j.nicl.2018.09.006.
18. Eide PK, Valnes LM, Lindstrøm EK, Mardal KA, Ringstad G. Direction and magnitude of cerebrospinal fluid flow vary substantially across central nervous system diseases. Fluids Barriers CNS. 2021;18(1):16. https://doi.org/10.1186/s12987-021-00251-6.
19. Liu P, Fall S, Balédent O. Use of real-time phase-contrast MRI to quantify the effect of spontaneous breathing on the cerebral arteries. NeuroImage. 2022;258:119361. https://doi.org/10.1016/j.neuroimage.2022.119361.
20. Liu P, Owashi K, Monnier H, Metanbou S, Capel C, Balédent O. Validating the accuracy of real-time phase-contrast MRI and quantifying the effects of free breathing on cerebrospinal fluid dynamics. Fluids Barriers CNS. 2024;21(1):25. https://doi.org/10.1186/s12987-024-00520-0.
21. Töger J, Andersen M, Haglund O, Kylkilahti TM, Lundgaard I, Markenroth Bloch K. Real-time imaging of respiratory effects on cerebrospinal fluid flow in small diameter passageways. Magn Reson Med. 2022;88(2):770–86. https://doi.org/10.1002/mrm.29248.
22. Sakhare AR, Barisano G, Pa J. Assessing test-retest reliability of phase contrast MRI for measuring cerebrospinal fluid and cerebral blood flow dynamics. Magn Reson Med. 2019;82(2):658–70. https://doi.org/10.1002/mrm.27752.
23. Vikner T, Karalija N, Eklund A, et al. 5-Year associations among cerebral arterial pulsatility, Perivascular Space Dilation, and White Matter lesions. Ann Neurol. 2022;92(5):871–81. https://doi.org/10.1002/ana.26475.
24. Björnfot C, Eklund A, Larsson J, et al. Cerebral arterial stiffness is linked to white matter hyperintensities and perivascular spaces in older adults - a 4D flow MRI study. J Cereb Blood Flow Metab off J Int Soc Cereb Blood Flow Metab Published Online Febr. 2024;5:271678X241230741. https://doi.org/10.1177/0271678X241230741.
25. Rivera-Rivera LA, Cody KA, Eisenmenger L, et al. Assessment of vascular stiffness in the internal carotid artery proximal to the carotid canal in Alzheimer's disease using pulse wave velocity from low rank reconstructed 4D flow MRI. J Cereb Blood Flow Metab off J Int Soc Cereb Blood Flow Metab. 2021;41(2):298–311. https://doi.org/10.1177/0271678X20910302.
26. Rivera-Rivera LA, Cody KA, Rutkowski D, et al. Intracranial vascular flow oscillations in Alzheimer's disease from 4D flow MRI. NeuroImage Clin. 2020;28:102379. https://doi.org/10.1016/j.nicl.2020.102379.
27. Rivera-Rivera LA, Vikner T, Eisenmenger L, Johnson SC, Johnson KM. Four-dimensional flow MRI for quantitative assessment of cerebrospinal fluid dynamics: Status and opportunities. NMR Biomed Published Online Dec. 2023;20:e5082. https://doi.org/10.1002/nbm.5082.
28. Stadlbauer A, Salomonowitz E, Brenneis C, et al. Magnetic resonance velocity mapping of 3D cerebrospinal fluid flow dynamics in hydrocephalus: preliminary results. Eur Radiol. 2012;22(1):232–42. https://doi.org/10.1007/s00330-011-2247-7.
29. Takizawa K, Matsumae M, Hayashi N, Hirayama A, Yatsushiro S, Kuroda K. Hyperdynamic CSF motion profiles found in idiopathic normal pressure hydrocephalus and Alzheimer's disease assessed by fluid mechanics derived from magnetic resonance images. Fluids Barriers CNS. 2017;14(1):29. https://doi.org/10.1186/s12987-017-0077-y.
30. Yamada S, Ishikawa M, Ito H, et al. Cerebrospinal fluid dynamics in idiopathic normal pressure hydrocephalus on four-dimensional flow imaging. Eur Radiol. 2020;30(8):4454–65. https://doi.org/10.1007/s00330-020-06825-6.
31. Yamada S, Otani T, Ii S, et al. Modeling cerebrospinal fluid dynamics across the entire intracranial space through integration of four-dimensional flow and intravoxel incoherent motion magnetic resonance imaging. Fluids Barriers CNS. 2024;21:47. https://doi.org/10.1186/s12987-024-00552-6.
32. Bunck AC, Kröger JR, Jüttner A, et al. Magnetic resonance 4D flow characteristics of cerebrospinal fluid at the craniocervical junction and the cervical spinal canal. Eur Radiol. 2011;21(8):1788–96. https://doi.org/10.1007/s00330-011-2105-7.
33. Heidari Pahlavian S, Bunck AC, Thyagaraj S, et al. Accuracy of 4D Flow Measurement of Cerebrospinal Fluid Dynamics in the cervical spine: an in Vitro Verification against Numerical Simulation. Ann Biomed Eng. 2016;44(11):3202–14. https://doi.org/10.1007/s10439-016-1602-x.
34. Jaeger E, Sonnabend K, Schaarschmidt F, Maintz D, Weiss K, Bunck AC. Compressed-sensing accelerated 4D flow MRI of cerebrospinal fluid dynamics. Fluids Barriers CNS. 2020;17:43. https://doi.org/10.1186/s12987-020-00206-3.
35. Johnson SC, Koscik RL, Jonaitis EM, et al. The Wisconsin Registry for Alzheimer's Prevention: a review of findings and current directions. Alzheimers Dement Amst Neth. 2018;10:130–42. https://doi.org/10.1016/j.dadm.2017.11.007.
36. Jack CR, Bennett DA, Blennow K, et al. NIA-AA Research Framework: toward a biological definition of Alzheimer's disease. Alzheimers Dement J Alzheimers Assoc. 2018;14(4):535–62. https://doi.org/10.1016/j.jalz.2018.02.018.
37. McKhann G, Drachman D, Folstein M, Katzman R, Price D, Stadlan EM. Clinical diagnosis of Alzheimer's disease: report of the NINCDS-ADRDA Work Group under the auspices of Department of Health and Human Services Task Force on Alzheimer's Disease. Neurology. 1984;34(7):939–44. https://doi.org/10.1212/wnl.34.7.939.
38. McKhann GM, Knopman DS, Chertkow H, et al. The diagnosis of dementia due to Alzheimer's disease: recommendations from the National Institute on Aging-Alzheimer's Association workgroups on diagnostic guidelines for Alzheimer's disease. Alzheimers Dement J Alzheimers Assoc. 2011;7(3):263–9. https://doi.org/10.1016/j.jalz.2011.03.005.
39. Albert MS, DeKosky ST, Dickson D, et al. The diagnosis of mild cognitive impairment due to Alzheimer's disease: recommendations from the National Institute on Aging-Alzheimer's Association workgroups on diagnostic guidelines for Alzheimer's disease. Alzheimers Dement J Alzheimers Assoc. 2011;7(3):270–9. https://doi.org/10.1016/j.jalz.2011.03.008.
40. Sperling RA, Aisen PS, Beckett LA, et al. Toward defining the preclinical stages of Alzheimer's disease: recommendations from the National Institute on Aging-Alzheimer's Association workgroups on diagnostic guidelines for Alzheimer's disease. Alzheimers Dement J Alzheimers Assoc. 2011;7(3):280–92. https://doi.org/10.1016/j.jalz.2011.03.003.
41. Langhough Koscik R, Hermann BP, Allison S, et al. Validity evidence for the Research Category, cognitively unimpaired - declining, as a risk marker for mild cognitive impairment and Alzheimer's Disease. Front Aging Neurosci. 2021;13:688478. https://doi.org/10.3389/fnagi.2021.688478.
42. Betthauser TJ, Koscik RL, Jonaitis EM, et al. Amyloid and tau imaging biomarkers explain cognitive decline from late middle-age. Brain J Neurol. 2020;143(1):320–35. https://doi.org/10.1093/brain/awz378.
43. Jonaitis EM, Janelidze S, Cody KA, et al. Plasma phosphorylated tau 217 in preclinical Alzheimer's disease. Brain Commun. 2023;5(2):fcad057. https://doi.org/10.1093/braincomms/fcad057.
44. Gu T, Korosec FR, Block WF, et al. PC VIPR: a high-speed 3D phase-contrast method for flow quantification and high-resolution angiography. AJNR Am J Neuroradiol. 2005;26(4):743–9.
45. Johnson KM, Markl M. Improved SNR in phase contrast velocimetry with five-point balanced flow encoding. Magn Reson Med. 2010;63(2):349–55. https://doi.org/10.1002/mrm.22202.
46. Fischl B, FreeSurfer. NeuroImage. 2012;62(2):774–81. https://doi.org/10.1016/j.neuroimage.2012.01.021.
47. Bernstein MA, Zhou XJ, Polzin JA, et al. Concomitant gradient terms in phase contrast MR: analysis and correction. Magn Reson Med. 1998;39(2):300–8. https://doi.org/10.1002/mrm.1910390218.
48. Loecher M, Schrauben E, Johnson KM, Wieben O. Phase unwrapping in 4D MR flow with a 4D single-step laplacian algorithm. J Magn Reson Imaging JMRI. 2016;43(4):833–42. https://doi.org/10.1002/jmri.25045.
49. Roberts GS, Hoffman CA, Rivera-Rivera LA, Berman SE, Eisenmenger LB, Wieben O. Automated hemodynamic assessment for cranial 4D flow

MRI. Magn Reson Imaging. 2023;97:46–55. https://doi.org/10.1016/j.mri.2022.12.016.
50. Vikner T, Nyberg L, Holmgren M, Malm J, Eklund A, Wåhlin A. Characterizing pulsatility in distal cerebral arteries using 4D flow MRI. J Cereb Blood Flow Metab off J Int Soc Cereb Blood Flow Metab. 2020;40(12):2429–40. https://doi.org/10.1177/0271678X19886667.
51. Stadlbauer A, Salomonowitz E, van der Riet W, Buchfelder M, Ganslandt O. Insight into the patterns of cerebrospinal fluid flow in the human ventricular system using MR velocity mapping. NeuroImage. 2010;51(1):42–52. https://doi.org/10.1016/j.neuroimage.2010.01.110.
52. Lee JH, Lee HK, Kim JK, Kim HJ, Park JK, Choi CG. CSF Flow quantification of the cerebral aqueduct in normal volunteers using phase contrast cine MR Imaging. Korean J Radiol. 2004;5(2):81–6. https://doi.org/10.3348/kjr.2004.5.2.81.
53. Ringstad G, Emblem KE, Geier O, Alperin N, Eide PK. Aqueductal Stroke volume: comparisons with intracranial pressure scores in idiopathic normal pressure Hydrocephalus. Am J Neuroradiol. 2015;36(9):1623–30. https://doi.org/10.3174/ajnr.A4340.
54. Yatsushiro S, Sunohara S, Hayashi N, et al. Cardiac-driven pulsatile motion of Intracranial Cerebrospinal Fluid visualized based on a correlation mapping technique. Magn Reson Med Sci. 2017;17(2):151–60. https://doi.org/10.2463/mrms.mp.2017-0014.
55. Fultz NE, Bonmassar G, Setsompop K, et al. Coupled electrophysiological, hemodynamic, and cerebrospinal fluid oscillations in human sleep. Science. 2019;366(6465):628–31. https://doi.org/10.1126/science.aax5440.
56. Dreha-Kulaczewski S, Joseph AA, Merboldt KD, Ludwig HC, Gärtner J, Frahm J. Inspiration is the major regulator of human CSF flow. J Neurosci off J Soc Neurosci. 2015;35(6):2485–91. https://doi.org/10.1523/JNEUROSCI.3246-14.2015.

Publisher's note